AIAA Aviation
22-26 June 2015, Dallas, TX
46th AIAA Plasmadynamics and Lasers Conference

Wavefront Measurements of a Supersonic Boundary Layer Using a Laser-Induced Breakdown Spark

Minh Nguyen[1], R. Mark Rennie[2], Stanislav Gordeyev[3], Eric J. Jumper[4]
University of Notre Dame, Notre Dame, Indiana, 46545

Alan B. Cain[5]
Innovative Technology Applications Co., Chesterfield, MO, 63006

Timothy E. Hayden[6]
U.S. Air Force Academy, Colorado Springs, Colorado 80840

The aero-optical effect of a flat-plate adiabatic boundary layer has been measured using the light generated by a laser-induced breakdown (LIB) spark. The measurements were performed in a blowdown wind tunnel at freestream Mach numbers of 3 and 4.38. The tests showed that the aero-optical effect of boundary layers with OPD_{rms} as low as 0.05 μm could be accurately measured using the LIB spark, including their deflection-angle amplitude spectra. The measurements demonstrate that using the LIB spark as a source of illumination, it is possible to make accurate measurements of low-amplitude aero-optical effects that are self-contained, non-intrusive, and suitable for a flight-test environment.

Nomenclature

δ	=	boundary layer thickness	r	=	radial coordinate
ε	=	small displacement	t	=	time
θ	=	small-aperture deflection angle	P_t	=	total pressure
$\hat{\theta}$	=	deflection angle amplitude spectrum	St_δ	=	Strouhal number based on δ
ρ	=	density	St_{MIN}	=	minimum resolvable Strouhal number
C_f	=	coefficient of skin friction	U	=	flow velocity
d_{AP}	=	aperture diameter	U_c	=	disturbance convection velocity
d_s	=	spark location from tunnel wall	W	=	wavefront
D_c	=	collimating lens diameter	x	=	stream-wise coordinate
f_c	=	collimating lens focal length	$\vec{x}$	=	position vector
f_{samp}	=	sampling frequency	y	=	cross-stream coordinate
K_{GD}	=	Gladestone-Dale constant	z	=	x cross y coordinate
M	=	Mach number	∞	=	(subscript) freestream conditions
n	=	index of refraction	rms	=	(subscript) root-mean-square
OPD	=	optical path difference			

[1] Graduate Research Assistant, Department of Mechanical and Aerospace Engineering, Hessert Laboratory for Aerospace Research, Notre Dame, IN 46556, Student Member AIAA.
[2] Research Associate Professor, Department of Mechanical and Aerospace Engineering, Hessert Laboratory for Aerospace Research, Notre Dame, IN 46556, Senior Member AIAA.
[3] Research Associate Professor, Department of Mechanical and Aerospace Engineering, Hessert Laboratory for Aerospace Research, Notre Dame, IN 46556, Senior Member AIAA.
[4] Professor, Department of Mechanical and Aerospace Engineering, Hessert Laboratory for Aerospace Research, Notre Dame, IN 46556, Fellow AIAA.
[5] President, Innovative Technology Applications Company, Chesterfield, MO 63006, Associate Fellow AIAA.
[6] Aerospace Engineer, Department of Aeronautics, Senior Member AIAA.

I. Introduction

THE wavefront of a beam of light passing through a compressible flow is distorted by spatial and temporal variations of the refractive index within the flow. The refractive-index variations are related to density variations by the Gladstone-Dale relationship:

$$n(\vec{x},t) = 1 + K_{GD}\rho(\vec{x},t) \tag{1}$$

where the Gladstone-Dale constant K_{GD} has a value of approximately $2.27\text{x}10^{-4}$ m^3/kg for light at visible and near-IR wavelengths. The optical distortion on a beam of light transiting the flow is then the average-removed integral of n along the distance traversed by the light beam:

$$OPD(x,y,t) = \int n'(x,y,z,t)dz \tag{2}$$

where OPD is the optical path difference, prime denotes mean-removed fluctuations, and propagation in the z direction is assumed. The study of the optical effect of compressible flows is called "aero optics." Examples of recent investigations into the aero-optical effects of boundary layers, shear layers and shock waves are described in [1-5].

Aero-optical effects are most commonly studied to evaluate their effect on airborne optical systems including directed-energy, imaging, or free-space communications systems. However, since the aberrations are the integrated effect of the flow density field, the aero-optical aberrations also contain valuable information on the underlying flow itself. The concept of determining flow properties by aero-optical measurement is especially relevant to recent development programs for new hypersonic flight vehicles (see, for example [6-8]). In this case, a key objective of ongoing hypersonic flight test is to measure boundary-layer parameters at hypersonic speeds [9-11]. As shown in [1,2], a flight-test measurement of the optical aberration imposed by the (turbulent) vehicle boundary layer could be related to boundary-layer thickness δ, local convection velocity, density, and other boundary-layer parameters. This kind of fluid-mechanic understanding cannot be obtained from ground-test and computational fluid dynamics (CFD) efforts alone, since ground-test facilities are not capable of achieving all points in the flight envelope of realistic flight-vehicle designs while CFD results require validation data.

Aero-optical measurement of a flight-test vehicle boundary layer also requires a source of light to provide the interrogating wavefront, that can be reliably generated at different locations in the flow around the flight vehicle. In this regard, an artificial light source for aero-optical measurements can be generated by focusing the output of an on-board laser to create a laser-induced breakdown (LIB) spark. A layout of a conceptual instrument to measure the aero-optical effect of the boundary layer on a flight-test vehicle is shown in Fig. 1; such an instrument would be both fully self-contained and nonintrusive.

Previous investigations into the use of a LIB spark as a light source for aero-optical measurements are described in [12 – 14]. In these investigations, the output of a pulsed Nd:YAG laser with wavelength of 355 nm was focused to create a LIB spark which was successfully used to measure the aero-optical aberrations produced by a compressible shear-layer flow. Due to the small scale of the wind tunnel used in these investigations, the LIB spark was formed in the quiescent laboratory air outside of the wind tunnel with the generated light directed through the wind-tunnel test section and shear-layer flow.

In this paper the results of an effort to measure the aero-optical effect of a boundary layer using the light from a LIB spark are presented. The investigation is significant in several respects. First, the measurements were performed at high supersonic Mach numbers closer to hypersonic flight-test speeds. Furthermore, the LIB spark was generated in the flow and therefore more-faithfully represents the kind of measurement that would be made during an actual flight-test deployment of the instrument. Finally, the magnitude of aero-optical distortion created by the boundary-layer flows under investigation were 1 to 2 orders of magnitude less than the shear-layer flows investigated in [12 – 14], so that the results of these tests represent a much more rigorous evaluation of the level of measurement sensitivity that can be achieved using the technique.

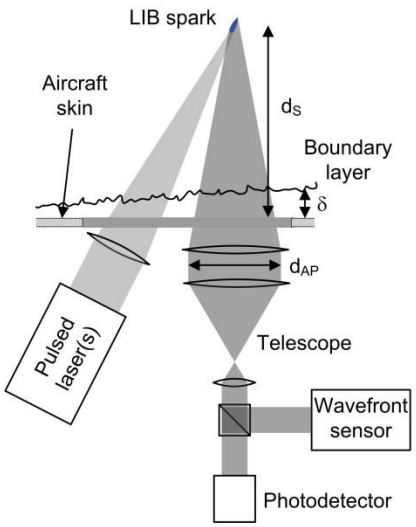

Fig. 1. Basic concept for optical instrument to measure aircraft boundary layer during flight test.

II. Experiment

Testing of the instrument was performed in the Trisonic Wind Tunnel (TWT) at the US Air Force Academy. This tunnel has a blowdown configuration with test-section dimensions of 1 ft x 1 ft, maximum Mach number of 4.38, and maximum test-section total pressure of 1.7 MPa. Air storage consists of six 25.5 m^3 tanks that can be pumped to a pressure of 4 MPa, giving up to 7 min of total run time depending on test conditions. The stored air is first dried to -45°C dewpoint and then heated to around 38°C in order to prevent water condensation, ice formation and/or liquefaction in the test section.

The measurements were performed at test-section Mach numbers of M_∞ = 3.0 and 4.38. Tunnel conditions for the experiments performed are summarized in Table 1. The boundary-layer thickness δ at the measurement location was estimated from the geometry of the wind-tunnel nozzles and a semi-empirical method described in [15], and was verified by Schlieren measurements. The standard-atmosphere altitude shown in Table 1 is based on the test-section density, which has the most effect on the magnitude of the aero-optic aberration produced by the boundary layer and hence signal strength of the measurements.

A. LIB Measurements

A schematic and photograph showing the integration of the optical setup for the LIB spark experiments into the TWT test section is shown in Fig. 2. The experiments were performed with an empty test section. A LIB spark was formed near the far wall of the test section by focusing a Nd:YAG pulsed laser with wavelength of 355 nm through a fused-silica window with good UV transmission properties. The advantage of the 355 nm wavelength is that, since the focal region of the focused laser beam becomes smaller as the wavelength is reduced, breakdown can be achieved with less pulse energy so that smaller LIB sparks can be formed which can improve the performance of the wavefront measurements.

Table 1. Summary of test conditions investigated for LIB spark measurements.

Parameter	Test 1 (T1)	Test 2 (T2)	Test 3 (T3)	Test 4 (T4)	Test 5 (T5)
Mach number	4.38	3.0	3.0	3.0	3.0
Total pressure (MPa)	1.5	1.4	1.0	0.7	0.5
Density (kg/m^3)	0.36	1.13	0.86	0.57	0.42
δ (mm)	26 ± 2.5	16 ± 1.5	16 ± 1.5	16 ± 1.5	16 ± 1.5
Effective altitude (km)	12.2	0.8	3.5	7.3	9.7

After passing through the wall boundary layer of the TWT test section, the light from the LIB spark was collected using a collimating lens (see Fig. 2), passed through a beam reducer, and into a high-speed wavefront sensor. The wavefront sensor consisted of a lenslet array with 38.1 mm focal length and 0.3 mm lenslet pitch attached to a high speed camera. The beam size on the CCD sensor was typically sized to span around 50 lenslets, with pixel resolution of ~15 pixels per lenslet. The sampling frequency of the measurements was 10 Hz, which was dictated by the pulse repetition rate of the Nd:YAG laser. The exposure time of the wavefront-sensor camera was also much longer than the 5 ns pulse duration of the laser, so that the wavefront sensor captured the full emission of the LIB spark. With this setup, the brightness of the LIB spark was not found to be a problem, with good wavefront measurements achieved using very small laser pulse energies on the order of 10 mJ/pulse.

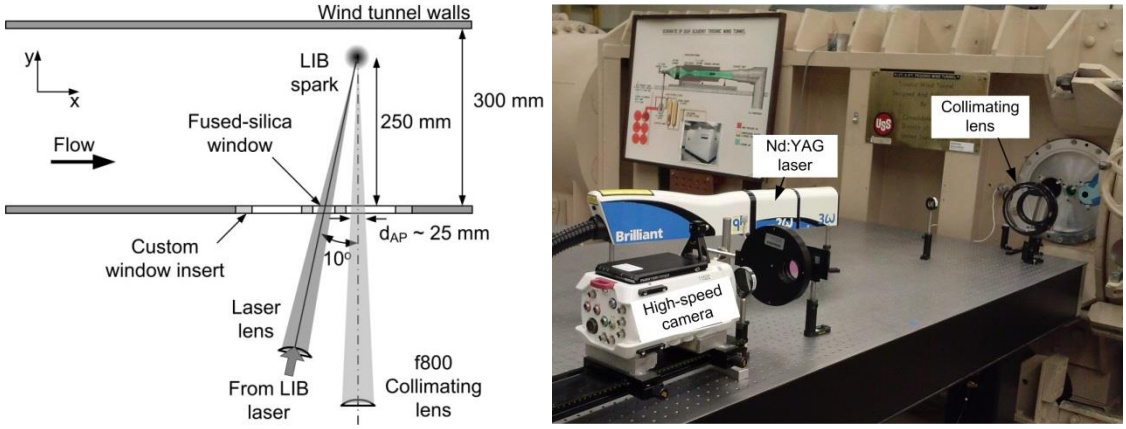

Fig. 2. Schematic (left), and photograph (right), of experiment to measure wall boundary layer of TWT using return light from an LIB spark.

B. CW Laser Measurements

Wavefront measurements of the TWT test-section boundary layer were also made using a continuous (CW) laser, and used to compare with the data obtained from the LIB spark setup. A schematic showing the setup for the experiments involving the CW laser is shown in Fig. 3. For the CW tests, a 532 nm wavelength light beam from the CW laser was first collimated and directed through either a 1 in. or 2 in. beam expander then passed through the empty test section normal to the optical-access windows. A return mirror on the other side of the test section was used to reflect the beam back through the test section and the beam expander and was split off into the wavefront sensor. The wavefront sensor consisted of a high-speed camera with a 38.1 mm focal-length lenslet array with 0.3 mm lenslet pitch.

In addition to acquisition of wavefronts over the full measurement aperture, high-speed CW measurements at a frame rate of 650 kHz were also made of only 11 focused dots from the lenslet array in order to more accurately resolve the high-frequency content of the boundary-layer aero-optical effect. An example of an image of the focused dots from the wavefront-sensor camera CCD array is shown in Fig. 4. In general, the CW measurements were performed at similar test conditions to the LIB tests summarized in Table 1. A full description of the methods and results of the CW measurements can be found in [16].

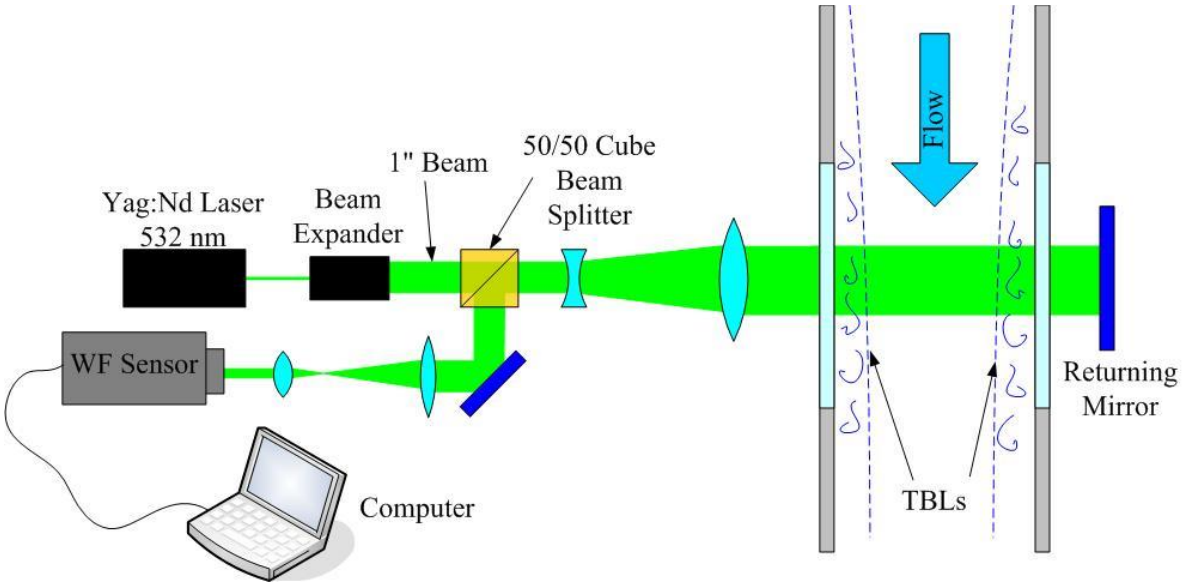

Fig. 3. Schematic of experiment to measure wall boundary layers of TWT using CW laser.

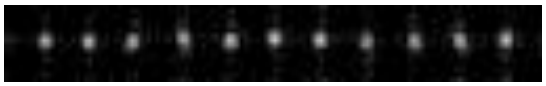

Fig. 4. Example of an image of focused dots acquired using CW test setup at 650 kHz sampling rate.

III. Results

Figure 5 shows an example of a single unprocessed image from the wavefront sensor acquired during measurements using the LIB spark as the light source. Note that each "dot" in the unprocessed image is actually an image of the LIB spark itself on the wavefront-sensor camera CCD array. Close inspection of Fig. 5 shows that the individual spark images become more elongated towards the edges of the measurement aperture. This elongation is the result of the different aspect of the LIB spark as "viewed" by the individual lenslets in the lenslet array, such that the spark appears elongated in the perspective of the lenslets located on the edge of the aperture. An analysis of how the wavefront measurements are affected by the size and shape of the LIB spark is given in [14].

The grey regions at the top and bottom of Fig. 5 represent regions of the camera CCD array that were outside of the extent of the lenslet array. These regions were removed by applying a circular aperture to the dot pattern, see Fig. 5. Wavefronts were then computed from the apertured dot patterns using standard methods. Specifically, an algorithm was used to identify the areas of interests (AOI's) for each data set, where each AOI contained a dot (i.e. spark image). The dot locations were next determined using a first-order centroiding calculation [17], and wavefront slopes were computed based on the dot deflections from their mean reference locations. Wavefronts were reconstructed from the wavefront slopes using the Southwell method [18], and optical tip, tilt and piston were removed from the wavefronts using a least-squares plane fitting calculation. Figure 5, right, shows a typical wavefront computed using this methodology.

A. Compensation for Spark Motion Effect

As shown in [14], a consequence of using the LIB spark for wavefront illumination is that the resulting wavefronts can be altered by the effect of motions of the LIB spark itself. Specifically, small motions in the exact location of spark formation, and/or variations in the shape of LIB spark, produce wavefronts of the spark emitted light that vary from ignition to ignition. These spark-produced wavefront distortions also appear in the measured wavefront data but are unrelated to the aero-optical effect of the flow under test.

As shown in [14], the wavefront distortions of the spark emitted light are well characterized by Zernike polynomials [19]. As an example, Fig. 6 [14] illustrates how small displacements ε of the spark towards or away from the focal point of the collimating lens result in a distortion of the spark emitted light that appears as the Zernike defocus mode (Zernike mode 4); note that examination of the sample wavefront shown in Fig. 5 clearly shows a

significant defocus component.

The effect of spark motion on typical wavefront data acquired using the LIB spark is illustrated by Fig. 7, which shows the first 40 Zernike coefficients for a typical set of wavefronts. Note that the Zernike coefficient for a mode represents the contribution of that mode to the overall root-mean-square of the spatial wavefront distortion, or OPD_{rms}. Included in the figure is an equivalent Zernike decomposition of a set of wavefronts acquired using the CW laser at the same Mach number and using the same size of measurement aperture. Figure 7 clearly shows that the spark wavefronts are affected primarily by defocus (Zernike mode 4) and smaller amounts of astigmatism (mode 6) and coma (mode 8). Diagrams of these three mode shapes are included on the right of Fig. 7.

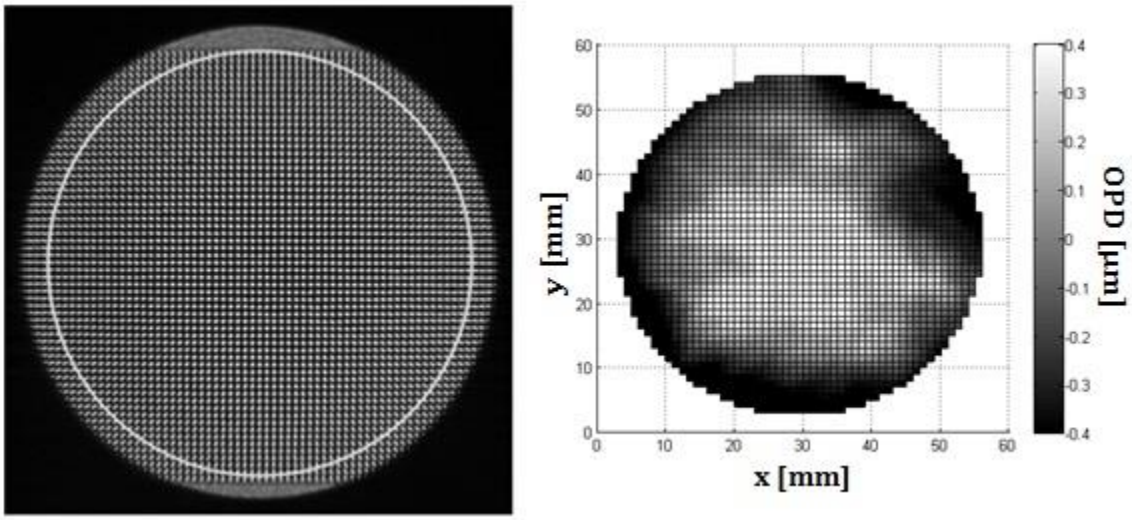

Fig. 5. Typical unprocessed dot pattern (left) from wavefront sensor (applied circular aperture outlined) and sample wavefront (right) computed from apertured dot pattern.

In general, aero-optical wavefront distortions produced by compressible boundary layers are very poorly represented by Zernike modes. This is because the radial and azimuthal symmetries of the Zernike mode shapes fail to capture the strong streamwise orientation of the boundary-layer aero-optical disturbances; this point is demonstrated by the slow convergence of the Zernike coefficients for the CW wavefront set shown in Fig. 7. As such, a first approach to removing the effect of LIB spark motion is to simply subtract the affected Zernike modes from the measured wavefronts. Figure 8 shows a sample of 9 wavefronts with Zernike modes 4, 6, and 8 removed. The wavefronts in Fig. 8 no longer show the strong defocus mode present in Fig. 5 right, and are clearly much more representative of boundary-layer aero-optical disturbances; specifically, they show dominant optical structure sizes on the order of the boundary-layer thickness in accordance with expected the boundary-layer aero-optical behavior described in [1,2].

In [1,2] the following model for the strength of the aero-optical aberrations produced by a flat-plate adiabatic boundary layer was developed:

$$OPD_{rms} = 0.2K_{GD}\rho_{\infty}M_{\infty}^{2}\delta\sqrt{C_f}F(M_{\infty}) \tag{3}$$

where $F(M_\infty)$ is the empirical function shown in Fig. 9. The OPD_{rms} that was computed for the full-aperture, CW measurements made at M_∞ = 3, 4.38 were also shown to match this model within experimental error, see points in Fig. 9 [16]. As shown in Table 1, Tests 2 to 5 were performed at M_∞ = 3 but at different total pressures and hence static densities; a plot of the OPD_{rms} for the data acquired using the LIB spark for these tests, and with Zernike modes 4, 6 and 8 removed, is shown in Fig. 10. The figure includes Eq.(3), and shows that the LIB results also match the model within experimental uncertainty. The result of Figs. 8 and 10 shows that it is possible to make accurate measurements of boundary-layer optical distortions using the LIB spark at altitudes up to at least the maximum shown in Table 1, where the local air density and hence strength of the optical signal is significantly reduced.

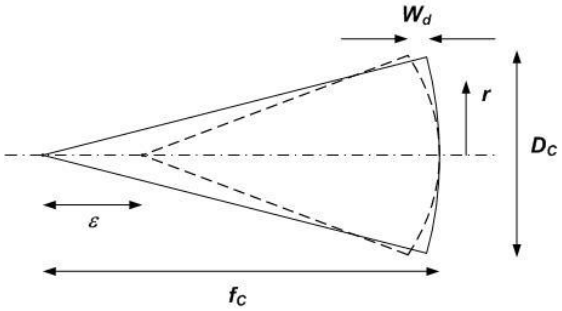

Fig. 6. Schematic showing how small displacements ε of the LIB spark towards or away from the collimating lens produce residual defocus on the measured wavefront.

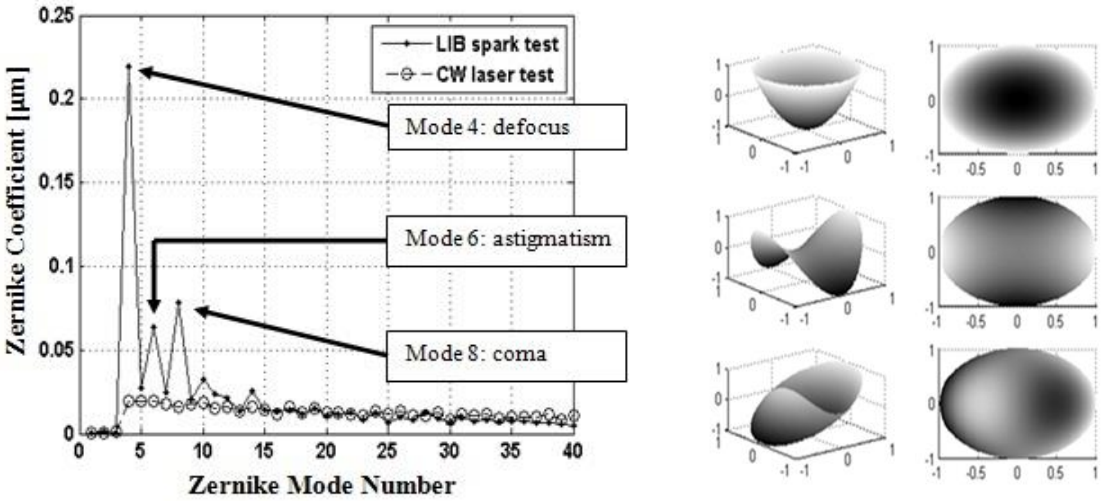

Fig. 7. Zernike coefficients for a dataset acquired at $M_\infty = 3.0$, $P_t = 1.0$ MPa (left) and diagrams of Zernike modes 4, 6, and 8 (right).

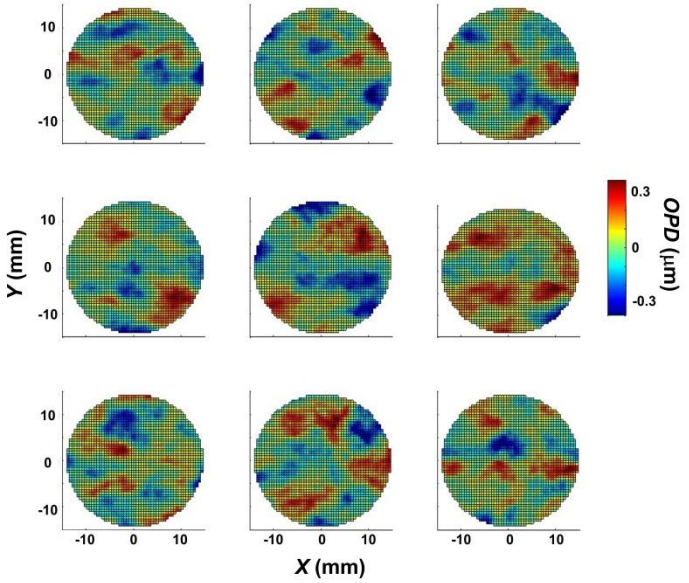

Fig. 8. Example set of 9 spark wavefronts with Zernike modes 4, 6 and 8 removed for $M_\infty = 3.0$, $P_t = 1.4$ MPa, $\delta = 16$ mm.

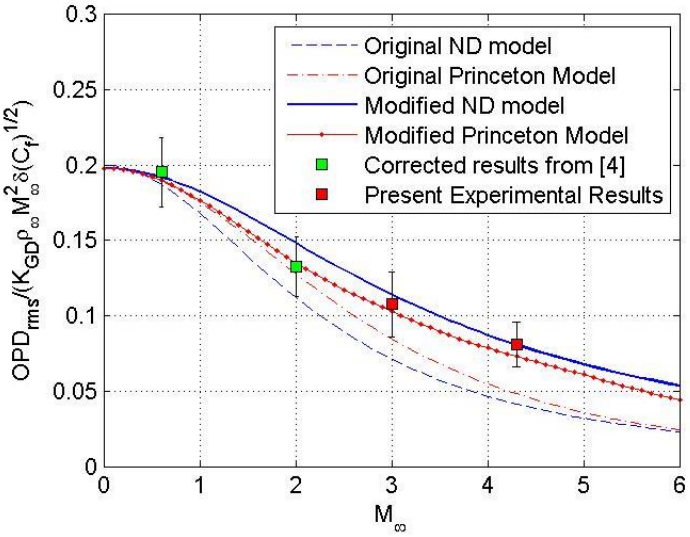

Fig. 9. Empirical function $F(M_\infty)$ for OPD_{rms} of aero-optical effect of flat-plate, adiabatic boundary layer [1, 2, 16].

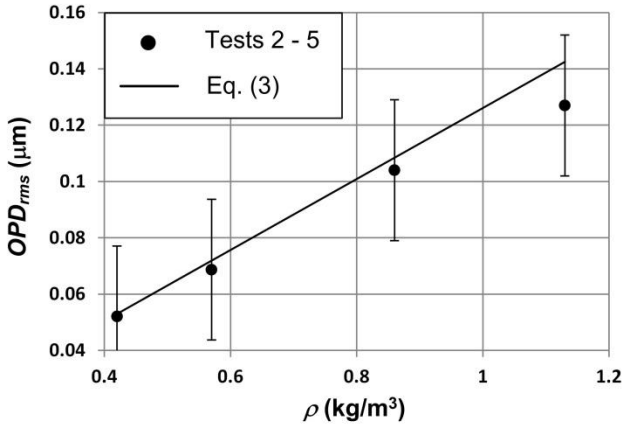

Fig. 10. Spatial OPD_{rms} for tests 2 to 5 in Table 1, with Zernike modes 4, 6 and 8 removed prior to computing OPD_{rms}.

B. Deflection-Angle Amplitude Spectrum

A useful result of aero-optical measurements is the deflection-angle amplitude spectrum $\hat{\theta}(f)$ [1, 2], which is the spectral decomposition of the deflection angle that a small-aperture light beam would have as it passes through the optically-active flow. The deflection-angle amplitude spectrum is typically calculated from measurements of the motion of the image of one or more small-aperture light beams acquired at sufficiently-high rate to resolve the spectral content of the boundary-layer aero-optical effect. However, since the sampling rate of the LIB measurements is limited to 10 Hz by the pulse-repetition rate of the LIB laser, deflection-angle data for the LIB tests were instead estimated from the slope of the wavefront data dW/dx calculated along the centerline of individual wavefront snapshots in the streamwise direction (after removal of Zernike modes 4, 6 and 8), as depicted in Fig. 11. Via the frozen-flow assumption, $\theta(t)$ is then:

$$\theta(t) = U_C \frac{dW}{dx} \tag{4}$$

where U_c is the convection speed of aero-optical structures. For a flat-plate adiabatic boundary layer, U_c is shown in

[16] to be approximately 0.88 U_∞ for M_∞ = 3, increasing to 0.9 U_∞ for M_∞ = 4.38. Deflection-angle amplitude spectra were also calculated for the CW data from the measured time histories of the locations of the 11-dot images acquired at high sampling rate (see Fig. 4).

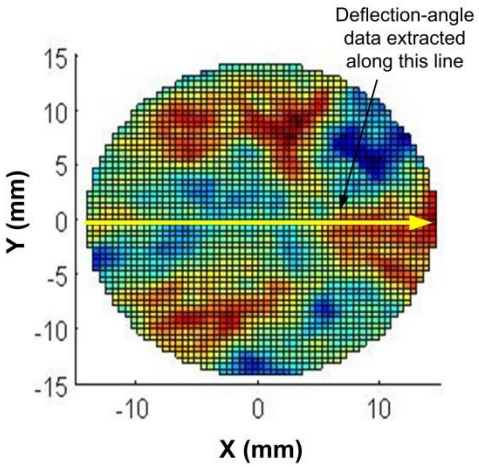

Fig. 11. Diagram illustrating how deflection-angle data were calculated along centerline of wavefronts acquired using LIB spark.

Deflection-angle amplitude spectra computed from the LIB-spark data and the CW data are shown in Fig. 12 for M_∞ = 3 and in Fig. 13 for M_∞ = 4.38. The spectra are plotted against the Strouhal number based on the boundary-layer thickness, St_δ. The figures show that the spectra computed from the individual LIB wavefronts, after removal of Zernike modes 4, 6 and 7, closely match the spectra calculated from the CW data using standard techniques.

Figures 12 and 13 show that the largest discrepancy between the LIB and CW spectra occurs for the the lowest-frequency components, where the LIB spectra generally show smaller amplitudes than the CW spectra. This discrepancy can be attributed to the removal of the low-order Zernike modes which was performed in order to compensate for the effects of LIB spark motion; for example, Fig. 14 shows curves extracted along the centreline of the Zernike modes 4, 6, and 7and clearly illustrates the low-frequency sinusoidal appearance of the modes. As such, complete removal of the Zernike modes 4, 6 and 7 from the LIB data could also unintentionally remove low-frequency components of the actual boundary-layer aero-optical effect. As shown in [1, 2, 16], the peak of the $\hat{\theta}(f)$ spectrum occurs at St_δ in the range 0.9 to 1. This means that, in situations where the measurements are performed on unknown flows in a flight-test environment, the inability to accurately resolve the low frequency components of $\hat{\theta}(f)$ using the LIB spark could detract from the ability to develop an accurate understanding of the boundary-layer aero-optical effect, especially if the lowest-frequency component(s) of $\hat{\theta}(f)$ occur in the range St_δ = 0.9 to 1.

For the method of determining $\hat{\theta}(f)$ from full-wavefront snapshots using the LIB spark, the minimum resolvable frequency component is the inverse of the time for an optical structure to traverse the full measurement aperture, U_c/d_{AP}. Creating a Strouhal number based on δ gives:

$$St_{\mathrm{MIN}} = \frac{\delta}{d_{AP}} \tag{5}$$

Equation (5) therefore shows that a simple approach to avoiding the effect of Zernike removal on $\hat{\theta}(f)$ is to use a measurement aperture large enough so that St_{MIN} is much lower than the lowest-frequency components of interest.

Alternatively, it may also be possible to better resolve the low-frequency components of $\hat{\theta}(f)$ using an improved approach to removing the effects of spark motion. Specifically, referring to Fig.7 it is clear that the boundary-layer aero-optical data acquired using the CW laser also contains nonzero magnitudes of the spark-affected Zernike modes; as such, fully removing these modes in an effort to remove the effects of spark motion is unrealistic. Instead, a more correct approach would be to attempt to reduce the magnitudes of the corrected modes to the levels that would exist normally, that is, the levels measured using the CW illumination. Using this approach, a more accurate amount of amplitude would be retained in the spark-affected modes, and also in the low-frequency

components of $\hat{\theta}(f)$.

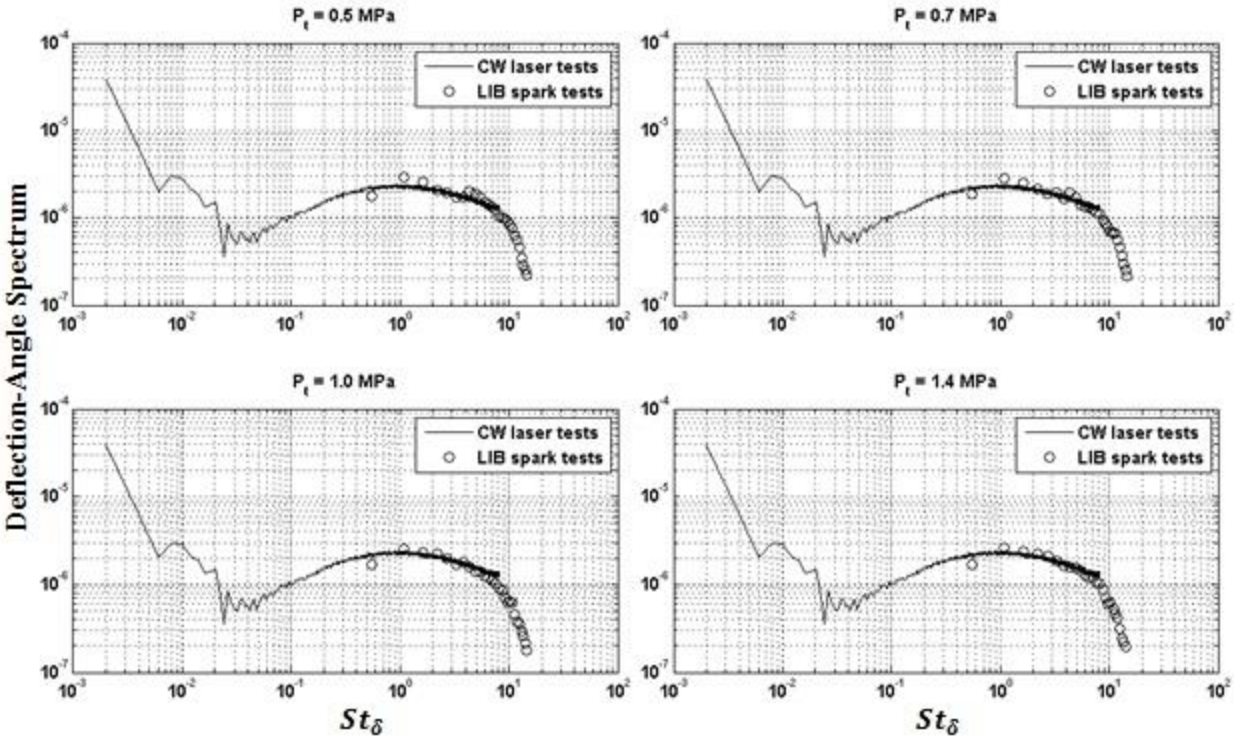

Fig. 12. Comparison of deflection-angle amplitude spectra computed from LIB data using method shown in Fig. 11 and after removal of spark-affected Zernike modes, with spectrum computed from CW tests, $M_\infty = 3.0$.

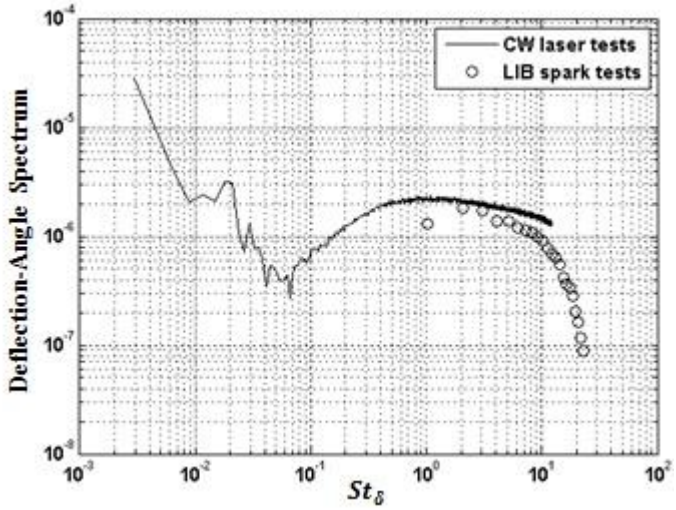

Fig. 13. Deflection angle spectra determined from LIB and CW tests, $M_\infty = 4.38$.

Furthermore, as shown in Fig. 7, the Zernike decomposition of the LIB and CW data closely match for all modes except for the few modes that are affected by spark motion. As such, the appropriate amplitude for the spark-affected modes can be estimated from a curve fit to the Zernike coefficients of the LIB wavefronts (excluding of course the modes affected by spark motion). This approach could then be used in situations where only LIB data are available, and could also deal with the possibility that the exact Zernike decomposition of the boundary-layer aero-optical effect may vary with the precise measurement details, for example, using different optical aperture sizes.

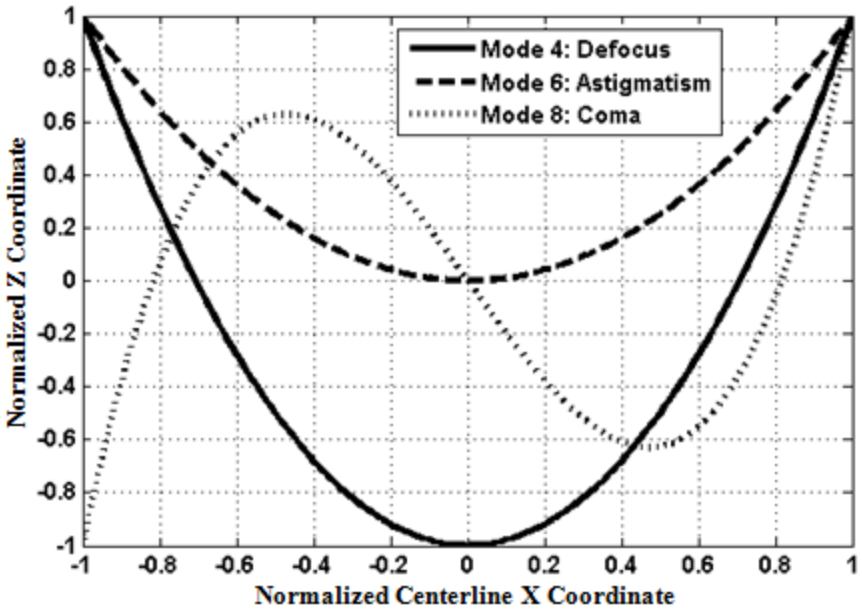

Fig. 14. Normalized plots along centreline of Zernike modes 4, 6, and 8.

An example of the kind of analysis described above is illustrated in Figs. 15 and 16. Figure 15 shows a curve fit to the Zernike modes that are unaffected by spark motion for a LIB data set; this curve fit was found to be well modelled using an exponential fit of the form ae^{bm} where m is the Zernike mode number. For comparison, Fig. 15 also includes the Zernike coefficients for a CW data set acquired at similar test conditions. The motion-affected Zernike modes for the LIB data set were then removed from the data down to the level of the curve fit, and the deflection-angle amplitude spectrum calculated. Figure 16 shows $\hat{\theta}(f)$ results for two LIB data sets, computed using the full-removal and the curve-fit methods of removing the spark-affected Zernike modes, and shows that the $\hat{\theta}(f)$ computed using the curve-fit method more closely match the CW spectra at low frequencies.

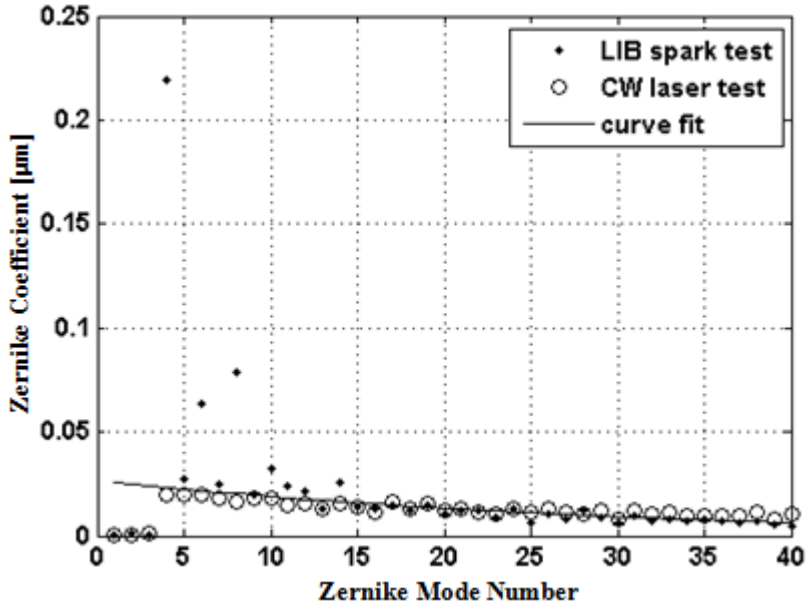

Fig. 15. Exponential fit to LIB spark Zernike coefficients and comparison to CW coefficients.

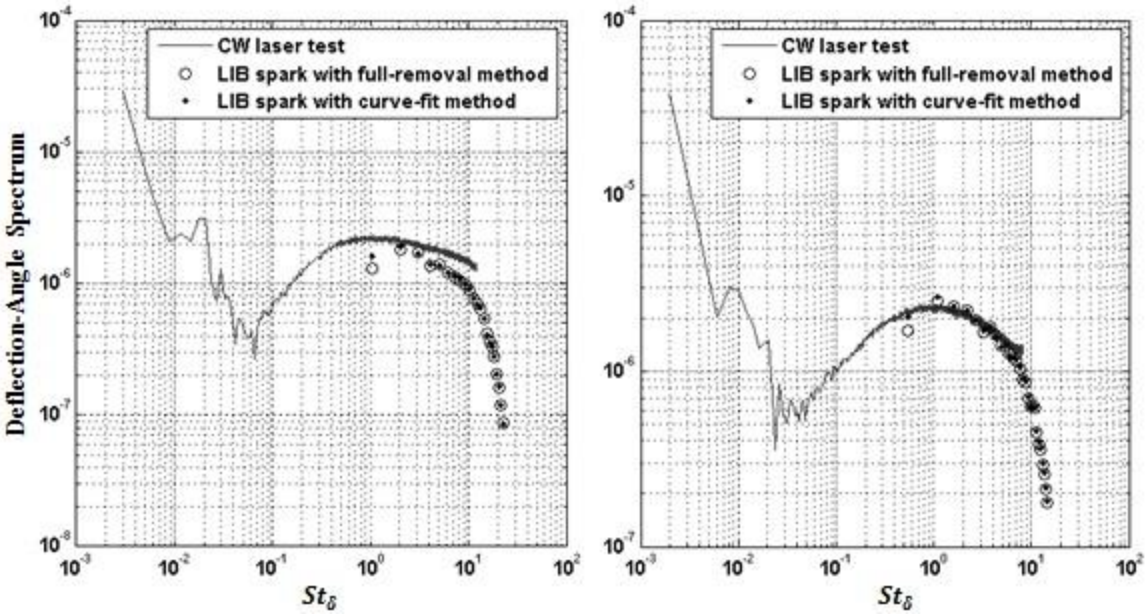

Fig. 16. Comparison of deflection-angle amplitude spectra computed using full removal of spark-affected Zernike modes, and by partial removal to the curve fit shown in Fig. 15, $M_\infty = 4.38$ and $P_t = 1.5$ MPa (left), $M_\infty = 3.0$ and $P_t = 1.4$ MPa (right).

IV. Concluding Remarks

The investigation has demonstrated that it is possible to accurately measure the aero-optical effects of flat-plate boundary-layer flows, including OPD_{rms} and deflection-angle amplitude spectra, using the light emitted by a LIB spark. A key step in the measurement technique is the handling of wavefront distortions caused by motion of the LIB spark itself. The investigation has shown that these wavefront distortions can be identified via a Zernike analysis and removed by subtraction of a few low-order Zernike modes such as defocus, coma and astigmatism, that are mainly affected by the spark motion.

More importantly, the investigation has shown that it is possible to measure very low optical signals using the LIB spark. Specifically, in this investigation, boundary-layer wavefronts with OPD_{rms} as low as 0.05 μm have been successfully measured using the LIB spark emission, corresponding to the expected aero-optical signal of a flat-plate boundary layer at an altitude of 12,000 m. This is especially significant if it is recognized that the measurements were made with only a single pass of the interrogating LIB light through the boundary-layer flow, in a manner that reproduces the kind of measurement that would be made in an actual flight-test situation; specifically, the LIB measurements described in the investigation did not (and could not in fact) take advantage of multiple passes of the interrogating light beam through the aero-optic flow in order to amplify the aero-optical signal. Furthermore, the measurements were also performed with the LIB spark formed in the flow, with no observed effect of the flow on the results.

Future efforts should continue to be directed toward methods of removing the effect of spark motion, or of eliminating it altogether if possible. For example, as indicated in [14] there is a relationship between the character of the LIB spark orientation and the resulting wavefront perturbation; as such, there may be a preferred orientation of the spark with respect to the flow that minimizes the influence of the spark motion effects on the measured aero-optical data.

Acknowledgments

This work has been supported by the United States Air Force Office of Scientific Research Contract Number FA9550-13-C-0010. The U.S. Government is authorized to reproduce and distribute reprints for governmental purposes notwithstanding any copyright notation thereon. Any opinions, findings and conclusions or recommendations expressed in this material are those of the authors and do not necessarily reflect the views of the AFOSR.

References

[1] S. Gordeyev, A. E. Smith, J.A. Cress and E.J. Jumper, "Experimental studies of aero-optical properties of subsonic turbulent boundary layers", *Journal of Fluid Mechanics*, 740, 2014, pp. 214-253.

[2] Gordeyev, S., Jumper, E.J., and Hayden, T.E., "Aero-Optical Effects of Supersonic Boundary Layers," *AIAA Journal*, Vol. 50, No. 3, 2012, pp. 682-690.

[3] Fitzgerald, E.J. and Jumper E.J., "The optical distortion mechanism in a nearly incompressible free shear layer," *Journal of Fluid Mechanics*, Vol. 512, 2004, pp. 153-189.

[4] Rennie, R.M., Duffin, D.A., and Jumper, Eric J., "Characterization and Aero-Optic Correction of a Forced Two-Dimensional, Weakly-Compressible Shear Layer," AIAA Journal, Vol. 46, No. 11, 2008, pp. 2787-2795.

[5] De Lucca, N., Gordeyev, S., and Jumper, E.J., " Comparison of Aero-Optical Measurements from the Flight Test of Full and Hemispherical Turrets on the Airborne Aero-Optics Laboratory", 43nd AIAA Plasmadynamics and Lasers Conference, 25 - 28 June 2012, New Orleans, Lousiana, AIAA Paper 2012-2985.

[6] Moses, P.L., Rausch, V.L., Nguyen, L.T., and Hill, J.R., "NASA hypersonic flight demonstrators—overview, status, and future plans," *Acta Astronautica*, Vol. 55, 2004, pp. 619 – 630.

[7] Canan, J.W., "Breathing new hope into hypersonics," *Aerospace America*, November, 2007, pp. 26-31.

[8] Croft, J., "Weapons delivery goes hypersonic," *Aerospace America*, May, 2004, pp. 38-42.

[9] Kimmel, R., Adamczak, D., and Gosse, R., "Ground Test and Computation of Boundary Layer Transition on the Hypersonic International Flight research and Experimentation (HIFiRE)-5 Vehicle," AFRL-RB-WP-TR-2011-3025, Feb., 2011.

[10] Kimmel, R., Adamczak, D., Gaitonde, D., Rougeux, A., and Hayes, J., "HIFiRE-1 Boundary Layer Transition Experiment Design," AIAA Paper 2007-0534, Jan., 2007.

[11] Berger, K., Rufer, S., Kimmel, R., and Adamczak, D., "Aerothermodynamic Characteristics of Boundary Layer Transition and Trip Effectiveness of the HIFiRE Flight 5 Vehicle,", AIAA Paper 2009-4055, June, 2009.

[12] Rennie, R. M., Whiteley, M. R., Cross, G., Cavalieri, D., and Jumper, E. J., "Optical Measurements of a Compressible Shear Layer Using a Laser-Induced Air Breakdown Beacon," AIAA Paper 2010-1158, Jan, 2010.

[13] Rennie, R.M., Goorskey, D., Whiteley, M.R., Cavalieri, D., and Jumper, E.J., "Evaluation of Laser Beacon for Adaptive-Optic Correction of a Compressible Shear Layer," *AIAA Journal*, Vol. 51, No. 4, 2013, pp. 1008-1011.

[14] Rennie, R.M., Goorskey, D., Whiteley, M.R., and Jumper, E.J., "Wavefront Measurements of a Laser-Induced Breakdown Spark in Still Air," *Applied Optics*, v.51, no.11, 2012.

[15] Stratford, B.S. and Beaver, G.S., The Calculation of the Compressible Turbulent Boundary layer in an Arbitrary Pressure Gradient – A Correlation of Certain Previous Methods, Reports and Memoranda No. 3207, Ministry of Aviation, Aeronautical Research Council, London, 1961.

[16] Gordeyev, S., Rennie, R.M., Cain, A.B., and Hayden, T.E., "Aero-Optical Measurements of High-Mach Supersonic Boundary Layers," 46th AIAA Plasmadynamics and Lasers Conference, Dallas, TX, June, 2015.

[17] A. M. Nightingale and S. Gordeyev, "Shack-Hartmann Wavefront Sensor Image Analysis: A Comparison of Centroiding Methods and Image Processing Techniques", *Journal of Optical Engineering*, 52(7), 071413, 2013.

[18] Southwell, W. H., "Wave-front estimation from wave-front slope measurements," Journal of the Optical Society of America, Vol. 70, No. 8, pp. 998-1006, 1980.

[19] Noll, R.J., "Zernike polynomials and atmospheric turbulence," *J. Opt. Soc. Am.*, Vol. 66, No. 3, March 1976.